IEEE Access
Multidisciplinary | Rapid Review | Open Access Journal

Received 2 June 2022, accepted 20 June 2022, date of publication 30 June 2022, date of current version 7 July 2022.

Digital Object Identifier 10.1109/ACCESS.2022.3187408

RESEARCH ARTICLE

Compact High-Selectivity Wide Stopband Microstrip Cross-Coupled Bandpass Filter With Spurline

TARUN KUMAR DAS[1], SAYAN CHATTERJEE[2], (Senior Member, IEEE), SHARUL KAMAL ABDUL RAHIM[3], (Senior Member, IEEE), AND TAN KIM GEOK[4]

[1]Department of ECE, Future Institute of Engineering and Management, Kolkata 700150, India
[2]Department of ETCE, Jadavpur University, Kolkata 700032, India
[3]Wireless Communication Centre, Universiti Teknologi Malaysia, Kuala Lumpur, Johor 81310, Malaysia
[4]Faculty of Engineering & Technology, Multimedia University, Malacca 75450, Malaysia

Corresponding author: Sayan Chatterjee (sayan1234@gmail.com)

This work was supported in part by Telekom Malaysia Berhad through a Research Grant under the Project with Title Transparent Filtering Antenna, Kementerian Pengajian Tinggi (KPT); and in part by Universiti Teknologi Malaysia under Grant 5F237, Grant 3F508, and Grant Q.J130000.21A2.05E25.

ABSTRACT The article presents the design of a compact narrowband microstrip cross-coupled bandpass filter with improved selectivity and a wide stopband. The proposed fourth-order quasi-elliptic filter is designed at 2.5 GHz with a fractional bandwidth of 4% suitable for WLAN applications. At first, doubly-folded half-wavelength hairpin lines have been arranged symmetrically in a cross-coupled configuration combining the electric, magnetic, and mixed-coupling. Accordingly, a size reduction of 17% over the folded inline hairpin-line filter with the same specifications has been achieved. Moreover, the selectivity has been improved greatly by the introduction of two deep transmission zeros with an attenuation level of 48 dB at the edges of the passband. However, the presence of the spurious harmonics with an attenuation level of 10 dB limits the performance of the filter related to the stopband rejection. As a remedy, conventional and meander spurlines have been incorporated in each hybrid coupled section of adjacent cross-coupled cells for achieving the modal phase velocity compensation. Accordingly, an extended stopband with a rejection level of 38 dB up to $4f_0$ has been recorded by using a meander spurline and an overall size reduction of 33% has been achieved.

INDEX TERMS Bandpass filter, high selectivity, harmonics suppression, spurline, wide stopband.

I. INTRODUCTION

In recent days Internet-of-things (IoT) provides the platform to allow big data transfer and communication between people and things worldwide. It supports the wireless local area network (WLAN) (IEEE 802.11/a/b/g/n) for 4G and 5G mobile communications. Narrowband bandpass filters are playing an important role in the transmitter and receiver module of IoT systems. However, with the continuous advancements in the modern IoT-based wireless communications systems, various functionalities are to be included and the size of the components is to be reduced accordingly. Hence, the demands for bandpass filters with compact size, narrowband, high selectivity, and wide stopband are increasing day by day for IoT applications. In this respect, microstrip parallel-coupled line and hairpin-line bandpass filters are good choices due to their ease of design and integration with other blocks [1]. However, the sizes of these two filters are pretty large, restricting their applications in IoT systems. Accordingly, the cross-coupled bandpass filters have been proposed by different researchers for the last decades due to their compact structures over the other two topologies. In the cross-coupled configuration electric, magnetic, and hybrid couplings are combined in a single structure akin to the only hybrid coupling for other topologies. As a result, the skirt selectivity of the filter has been improved greatly due to the placement

The associate editor coordinating the review of this manuscript and approving it for publication was Kashif Saleem.

of two sharp transmission zeros with a large attenuation level (greater than 30 dB) at the passband edges [2]–[8].

In this context, a compact-sized ($0.29\lambda_g \times 0.14\lambda_g$, λ_g is the guided wavelength at the center frequency) cross-coupled filter with an improved roll-off rate of 197.70 for the lower passband edge and 180.04 for the upper passband edge has been designed in [4] incorporating the 2nd iteration Minkowski fractals based defected ground structure (DGS) open-loop resonators. However, both the design and fabrication complexities have been increased for higher iteration order of fractals.

Later, in [5] a two-fold tunable cross-coupled open-loop resonator bandpass filter has been proposed. The center frequency of the proposed filter ranges from 1.5 GHz to 1.75 GHz, with a constant bandwidth of 100 MHz. The selectivity of the filter has been improved by placing two transmission zeros at the passband edges and the bandwidth has been tuned between 70 MHz and 180 MHz at a fixed center frequency of 1.625 GHz by using thin-film barium strontium titanate (BST) varactors. However, additional care is required for soldering the varactor diodes on the microstrip laminate. In this context, a compact-sized ($0.34\lambda_g \times 0.12\lambda_g$) four-pole wideband bandpass filter centered at 3.35 GHz has been proposed in [6] by providing combined electric and magnetic coupling for two dual-mode stub-loaded stepped-impedance resonators (SLSIRs).Very recently, a compact four-pole cross-coupled filter centered at 2.5 GHz has been designed in [7] by folding the conventional open-loop resonator. However, most of the works proposed in [2]–[7] have mainly focused on two factors: improvement of the skirt selectivity and the reduction of the filter's size. Thus, their applications are limited and are unsuitable for those applications where the harmonics create problems such as mixers, frequency synthesizers, etc.

The primary reason for the generation of harmonics is the inhomogeneous microstrip structure supporting quasi-TEM mode. As a result, the odd-mode of the EM wave propagates faster than the even-mode. Such imbalances of phase velocities have been compensated by incorporating different slow-wave structures in the cross-coupled filters. In [8], a size reduction of 44% has been achieved over the conventional bandpass filter by placing open-ended stubs at appropriate locations inside the open-loop cross-coupled resonators. A wide stopband of $3.2f_0$ with a rejection level of 26 dB has been obtained. Subsequently, a quasi-elliptic function cross-coupled filter has been designed in [9] with the folded stepped-impedance open-loop resonators. As a result, compact size of $0.21\lambda_g \times 0.20\lambda_g$ and a wide stopband up to $3f_0$ with a rejection level of 34 dB have been reported. As an alternative, a third-order quasi-elliptic function cross-coupled filter with a stopband rejection of 40 dB up to $2.44f_0$ has been proposed in [10]. The size of the filter is $0.21\lambda_g \times 0.20\lambda_g$. However, the stopband bandwidths are restricted to only $3.2f_0$ or less for the filters proposed in [8]–[10]. Accordingly, the stopband bandwidth has been extended up to $4.95f_0$ by utilizing the folded stepped-impedance microstrip lines with open stubs for a compact-sized ($0.24\lambda_g \times 0.35\lambda_g$) cross-coupled filter in [11]. However, the stopband rejection level has been recorded as only 24.5 dB for this work.

Very recently, a compact cross-coupled filter with a coupled line-stub cascaded structure has been proposed in [12]. The circuit area is $0.39\lambda_g \times 0.36\lambda_g$ and the stopband rejection level has been recorded as 28.9 dB up to $2.3f_0$. In [8]–[12] different folded open-loop resonator structures with open-ended stubs and stepped-impedance resonators have been employed to obtain a high degree of roll-off rate, compact size, and extended stopband with improved rejection level. All these structures require critical optimization of the length of the stubs and SIRs as proper high-to-low impedance ratio influences the harmonics suppression performance of such filters. As an alternative approach, slow-wave spurlines have been investigated in [13]–[15] along with SIRs. In [13] a wide stopband up to $3f_0$ with a suppression level of 30 dB and size reduction of 96% (size of $0.39\lambda_g \times 0.36\lambda_g$) over the conventional open-loop cross-coupled filter has been reported by selectively adjusting the dimensions of the spurline. Subsequently, short-stub-loaded dual-mode resonator (SSL-DMR) and stepped-impedance spurline resonators (SISLRs) have been adopted in [14] to design a compact-sized ($0.16\lambda_g \times 0.75\lambda_g$) filter. In [15], source-load-coupled spurlines have been embedded with SIRs to achieve an overall size of $0.129\lambda_g^2$ for the cross-coupled filter. For both the filters of [14], [15] stopband rejection bandwidth of $4f_0$ and the rejection level of 20 dB have been reported. However, there is a compromise between stopband rejection bandwidth and rejection level in [13]–[15]. Very recently, double-fold uniform impedance hairpin resonators have been placed in a cross-coupled configuration to design a compact filter (size of $0.22\lambda_g \times 0.25\lambda_g$) [16]. Subsequently, conventional spurlines with optimum dimensions have been incorporated to achieve the stopband bandwidth up to $3.16f_0$ and a rejection level of 35 dB.

In the present article, conventional spurlines of [16] have been modified by meander spurline to provide a higher degree of slow-wave effect for the signal and to achieve more phase velocity compensation for the same filter structure with the same specifications. The effectiveness of the meander spurline over the conventional spurline has been justified by the equivalent lumped elements analysis and two prototype filters with two different spurlines have been fabricated on FR4 substrate material having dielectric constant $\varepsilon_r = 4.4$, thickness $h = 1.6$ mm, and loss tangent $\tan\delta = 0.02$. As an experimental result, an extended stopband up to $4.3f_0$ with a rejection level of 41 dB has been achieved for the meander spurline-based filter.

II. DESIGN OF FOLDED CROSS-COUPLED FILTER

Quasi-elliptic filters generate one pair of transmission zeros at the edges of the passband, increasing the skirt selectivity to a high degree akin to the Chebyshev and elliptic filters. Typical cross-coupled filters require four open-loop quarter-wavelength resonators placed in electric, magnetic, and

TABLE 1. Specifications of the filter.

Parameters	Notations	Specifications
Mid-band Frequency	f_0	2.5 GHz
Fractional Bandwidth	FBW	4%
3 dB Bandwidth	BW	100MHz
Insertion Loss	IL	<3 dB
Passband Ripple	L_{Ar}	0.1 dB
Return Loss	RL	>15 dB

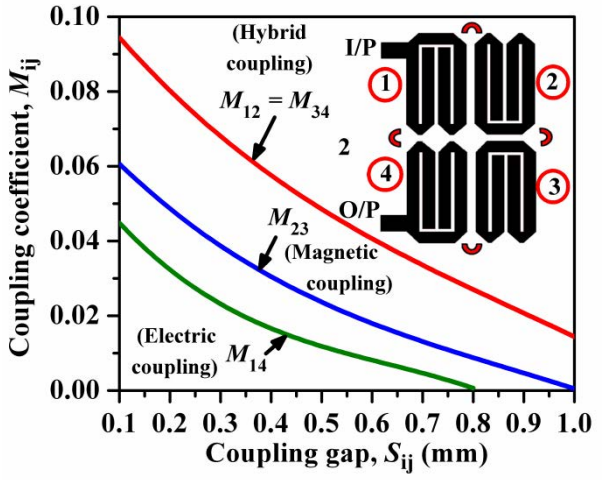

FIGURE 1. Variation of the coupling-coefficient vs. coupling gap for a pair of folded hairpin-line cells in different coupling configurations.

mixed-coupling configurations. However, the order of the filters is determined by the design specifications of the cross-coupled filters. But, the size of the filter will increase as the order increases, limiting its integration with other blocks of the transmitter and receiver in the wireless communication systems. The specifications of the quasi-elliptic type cross-coupled bandpass filter proposed in this work applicable for WLAN (IEEE 802.b) systems are listed in Table 1 [17].

The elements of the prototype low-pass filter with passband ripple of 0.1 dB has been obtained from [1] as $g_1 = 0.95974$, $g_2 = 1.42192$, $J_{14} = -0.21083$ and $J_{23} = 1.11769$. Accordingly, the external quality factors have been calculated as $Q_{e1} = Q_{e4} = 19.1948$ from (1) and the coupling coefficients between the adjacent coupled lines have been computed as $M_{1,2} = M_{3,4} = 0.0428$, $M_{2,3} = 0.0393$, $M_{1,4} = -0.0277$ from (2) - (4). From the design curve highlighted in Fig. 1 the initial values of the coupling gaps for the pair of adjacent cells have been determined as $S_{12} = S_{34} = 0.56$ mm, $S_{23} = 0.28$ mm, and $S_{14} = 0.8$ mm. Finally, the dimensions of the cross-coupled filter have been obtained optimally by performing the EM simulation in IE3D. Fig. 2 depicts the layout of the fourth-order cross-coupled filter. The size of the filter is 291.04 mm^2 i.e., $0.22\lambda_g \times 0.28\lambda_g$ where λ_g is the guided wavelength at the center frequency $f_0 = 2.5$ GHz. Fig. 3 highlights the simulated S-parameters plots of the cross-coupled

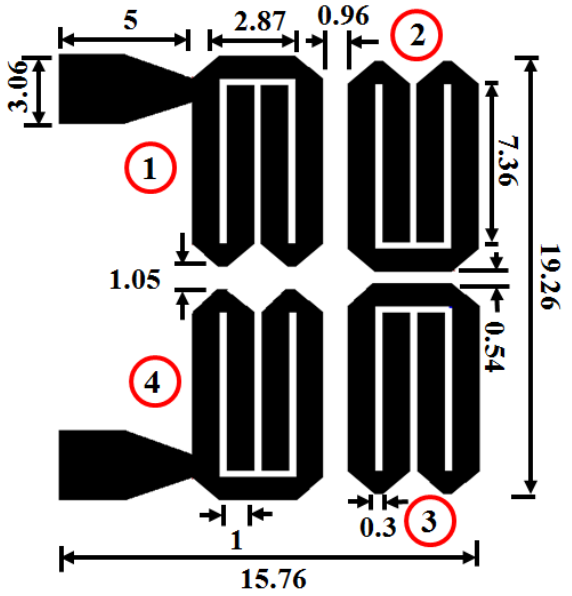

FIGURE 2. Layout of the fourth-order quasi-elliptic folded cross-coupled bandpass filter. All dimensions are in mm.

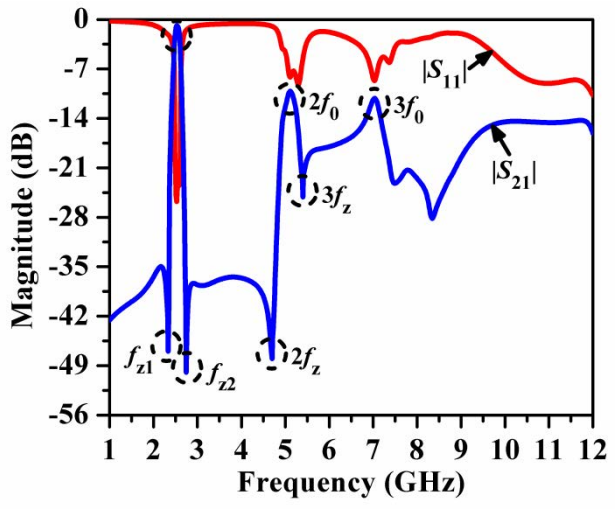

FIGURE 3. *S*-parameters plots of fourth-order cross-coupled filter.

bandpass filter.

$$Q_{ei} = Q_{eo} = \frac{g_1}{FBW} \tag{1}$$

$$M_{i,i+1} = M_{n-i,n-i+1} = \frac{FBW}{\sqrt{g_i g_{i+1}}} \tag{2}$$

$$M_{m,m+1} = \frac{FBW.J_m}{g_m} \tag{3}$$

$$M_{m-1,m+2} = \frac{FBW.J_{m-1}}{g_{m-1}} \tag{4}$$

It has been noticed that two sharp transmission zeros occurred at 2.33 GHz (f_{z1}) and 2.74 GHz (f_{z2}) with the attenuation levels of 47 dB and 51 dB respectively. The reason behind such behavior is due to the combinations of electric, magnetic and mixed coupling in the cross-coupled

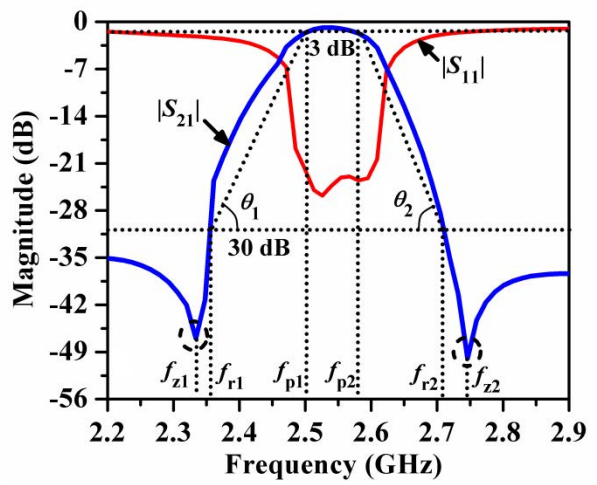

FIGURE 4. Calculation of shape factor and skirt selectivity factor.

structure. The insertion loss and the return loss have been obtained as 0.95 dB and 25 dB respectively. The skirt characteristics of the filter have been characterized by the following parameters: shape factor (*SF*) (dimensionless), roll-off slope factors (*ROSFs*) (dB/GHz), and transmission zero selectivity factor (*TZSF*) (dimensionless) as highlighted in Fig. 4. *SF* is the ratio of the 30 dB rejection bandwidth (f_{r2}-f_{r1}) to the 3 dB bandwidth (f_{p2}-f_{p1}) [1]. *ROSFs* are defined as the slope θ_1 for the lower passband (27 dB/ (f_{r2}-f_{p2}) GHz) and θ_2 for the upper passband (27 dB/ (f_{p1}-f_{r1}) GHz).

Finally, *TZSF* is the ratio of the center frequency f_0 to the difference between the transmission zero frequencies at the passband edges i.e., $TZSF = f_0/(f_{z2}\text{-}f_{z1})$. These values have been calculated from Fig. 4 as $SF = 2.5$, $ROSF = 245.45$ dB/GHz (for both lower and upper passband edges), $TZSF = 6.1$. It can be concluded that the value of *SF* is slightly higher than unity (ideal value), the passband response is quite symmetrical about f_0 as the *ROSF* values for both the lower and upper passband are same and the higher value of *TZSF* indicates the narrow bandwidth of the filter.

Although the passband response of the designed filter is quite satisfactory, however, two additional transmission zeros $2f_z$ and $3f_z$ have been occurred at 4.7 GHz and at 5.5 GHz with the attenuation levels of 47 dB and 24 dB respectively. The attenuation levels at $2f_0$ and $3f_0$ are less than 10 dB which restricts the proposed filter's applications in the WLAN system with respect to harmonics rejection performance. By following the conventional transmission line theory of microstrip line [1], the equivalent lumped elements circuit diagram of the fourth-order cross-coupled bandpass filter has been obtained in Fig. 5. The values of the lumped elements have been computed as $L_1 = 2.426$ nH, $L_2 = 3.011$ nH, $L_3 = L_6 = 1.169$ nH, $L_4 = L_5 = 3.685$ nH, $C_{p1} = C_{p2} = 0.167$ pF, $C_{p3} = C_{p8} = 0.287$ pF, $C_{p4} = C_{p5} = 0.083$ pF, $C_{p6} = C_{p7} = 0.275$ pF, $C_{g1} = C_{g2} = C_{g3} = 0.015$ pF, $C_{14} = 0.015$ pF, $C_{12} = C_{34} = 0.035$ pF, $C_{23} = 0.238$ pF. The comparison of EM and circuit simulated $|S_{21}|$ (dB) plot has been explored in Fig. 6. It has been observed that the plots are closely matched in the passband with the center frequency f_0. However, other harmonics' locations have not been matched perfectly. Moreover, eight transmission zeros have been occurred from 1.0 GHz and 12 GHz in circuit simulation and the corresponding attenuation levels are more than those for EM simulation. Such mismatches have been occurred due to the differences in the simulation platforms such as assumption of zero conductor loss and zero loss tangent ($\tan\delta$) for the substrate material in circuit simulation.

Another reason is the large propagation delays that occurred due to a large number of lumped elements connected in the final circuit. The entire simulation has been carried out with 50 Ohm feed port characteristic impedances. From the surface current vectors plots of Fig. 7(a)-(b), it has been observed that the density vectors have been propagated with a high degree of strength at $f_0 = 2.5$ GHz due to the passband and slightly less strength at $2f_0 = 5.0$ GHz due to the presence of the second harmonic. From the literature study of microstrip cross-coupled filters, it has been revealed that spurious harmonics are generated exclusively due to the even- and odd-mode phase velocities imbalance of the EM wave. Thus, different nonuniform perturbations have been incorporated by the researchers in the coupled region between the adjacent arms of the lines. In this context, spurline is one of the most attractive microstrip defects that effectively suppress the harmonics for parallel-coupled line filters [14], [15] and hairpin-line filters [18]–[20]. Hence, the next objective of the present work has been set to suppress the harmonic attenuation level below 35 dB while keeping the satisfactory passband response.

III. HARMONICS SUPPRESSION BY L-SPURLINE

In general, spurline is a microstrip defect created by etching one defected slot of L shaped in the microstrip line [18]. As shown in Fig. 8, a spurline is the combination of a pair of asymmetrical coupled lines connected at one end, and another end of the shorter line is etched away by a small gap g. In this way, the resonance property of the mainline has been changed by changing its inductive and capacitive properties. In general, the inductance of the line has been controlled by the length of the slot and the gap between the two coupled lines of the spurline will control the capacitance of the line. Thus, by properly adjusting the length of the spurline l_{sp} and the value of g, the resonant frequency of the bandstop response of the structure can be tuned properly with a large attenuation level. The spurline is characterized by its non-dispersive virtual behavior dominated by the odd-mode of the EM wave propagation. The physical length of the spurline has been determined by Bates as (5)-(6) [21]. In (5) c is the speed of light, ε_{effo} is the odd-mode effective dielectric constant, $\boldsymbol{Z}_{oo}$ is the odd-mode characteristic impedance, $\boldsymbol{C}_{end}$ is the open-end parasitic capacitance at resonance due to the gap

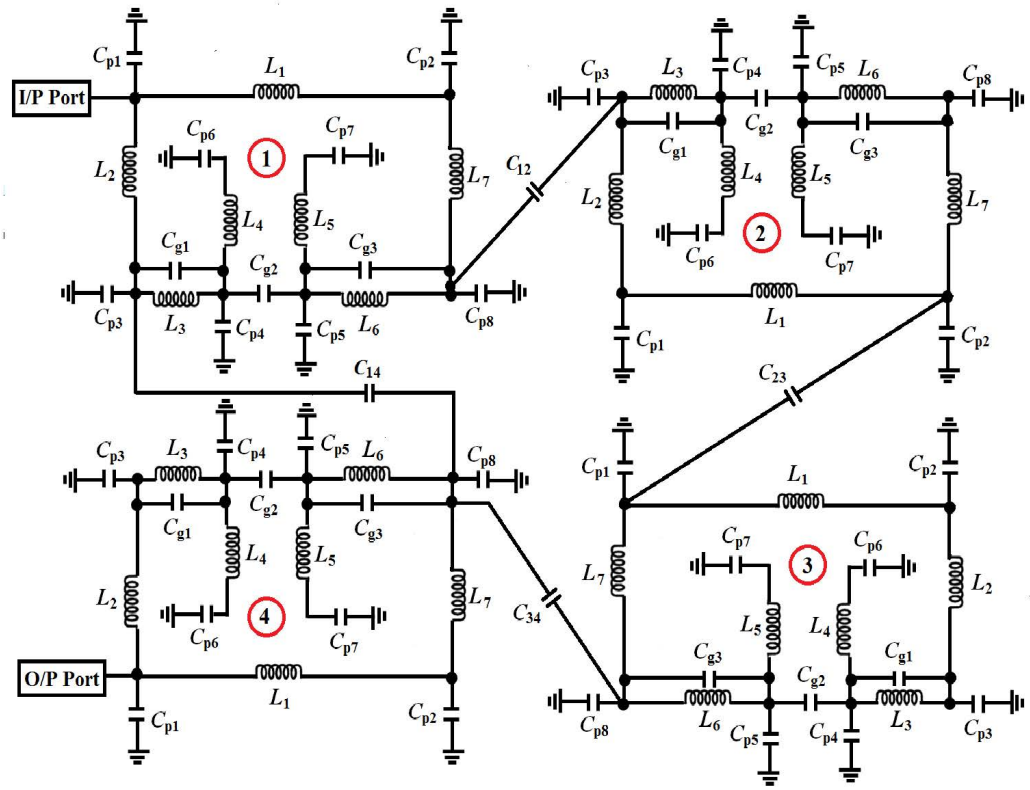

FIGURE 5. Equivalent lumped elements circuit diagram of the fourth-order cross-coupled bandpass filter.

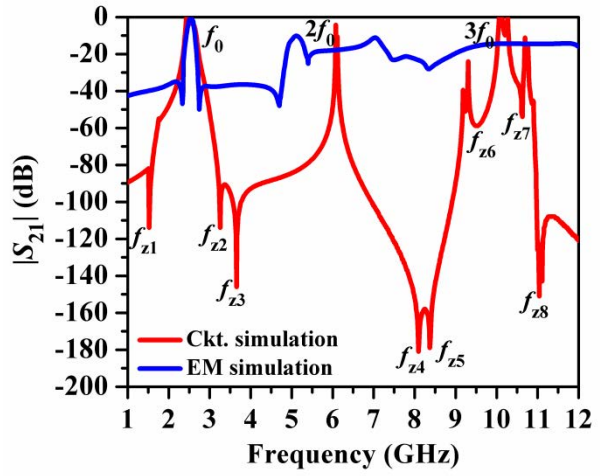

FIGURE 6. Comparison of EM and circuit simulated $|S_{21}|$ (dB) plot of the fourth-order cross-coupled bandpass filter.

g and Δl is the open-end length correction.

$$l_{sp} = \frac{c}{4f_0\sqrt{\varepsilon_{effo}}} - \Delta l \tag{5}$$

$$\Delta l = \frac{C_{end} Z_{oo} c}{\sqrt{\varepsilon_{effo}}} \tag{6}$$

Due to the microstrip slot, the odd-mode of the signal will propagate with lower phase velocity and the even-mode will propagate almost unaltered, resulting in phase velocity compensation. By following the typical transmission line theory [1] the equivalent circuit of the spurline has been obtained as shown in Fig. 9 [21].

$$R = 2Z_0(1/|S_{21}| - 1)|_{f=f_0} \tag{7}$$

$$C = \frac{\sqrt{0.5(R + 2Z_0)^2 - 4Z_0^2}}{2.83\pi Z_0 R \Delta f} \tag{8}$$

$$L = \frac{1}{4(\pi f_0)^2 C} \tag{9}$$

In the equivalent circuit of the spurline, R is the equivalent resistance caused by the radiation effect and conductor loss. L is the equivalent inductance of the spurline and C is the equivalent capacitance due to the coupling gap between the coupled lines and the open-end. The circuit parameters can be computed by equations (7)-(9) [20] as $L = 0.410$ nH, $C = 1.929$ pF, $R = 3.125$ kΩ by obtaining the value of $|S_{21}|$ as 44 dB from the resonant characteristics as highlighted in Fig. 10 for a quarter-wavelength resonator with L-spurline tuned at 2.5 GHz. It has been noticed from Fig. 10 that the EM simulated and the circuit simulated plots are in close agreement with each other. Fig. 11 illustrates the surface current distribution for a quarter-wavelength line with an L-spurline tuned at 2.5 GHz. It has been revealed that the current vectors are propagating through the upper and lower coupled lines in the opposite direction and vanish at the open-end. Accordingly, the study of the proposed cross-coupled

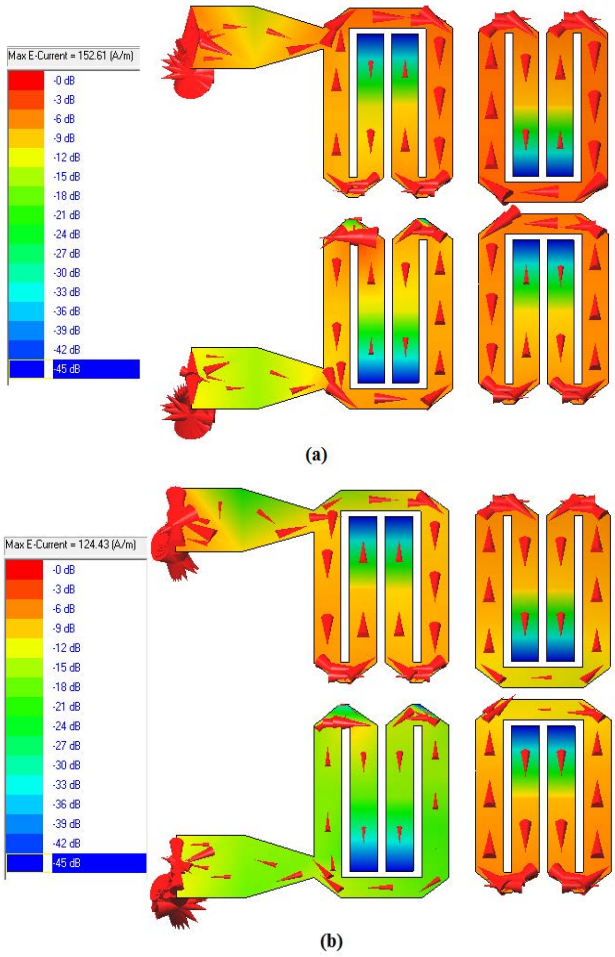

FIGURE 7. Distribution of surface current vectors for the fourth-order cross-coupled filter at (a) $f_0 = 2.5$ GHz, and (b) $2f_0 = 5.0$ GHz.

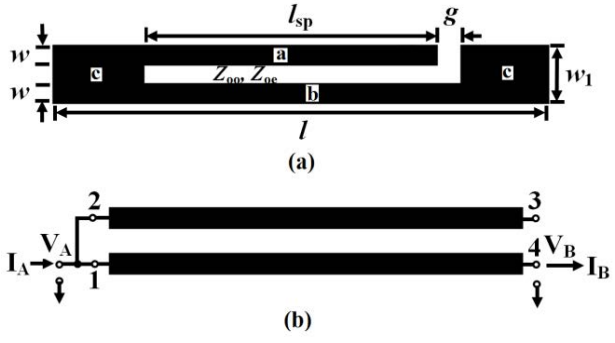

FIGURE 8. (a) Layout of the L-shaped spurline, (b) transmission line structure.

filter (Fig. 2) with spurlines has been investigated in the next section.

IV. FOURTH-ORDER CROSS-COUPLED FILTER WITH L-SPURLINE

The layout of the fourth-order cross-coupled filter with an *L*-shaped spurline is depicted in Fig. 12. The spurlines have been incorporated in the hybrid coupling region as highlighted by red dashed lines. The spurline length ratio α

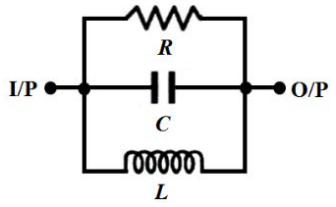

FIGURE 9. Equivalent lumped elements circuit diagram of spurline.

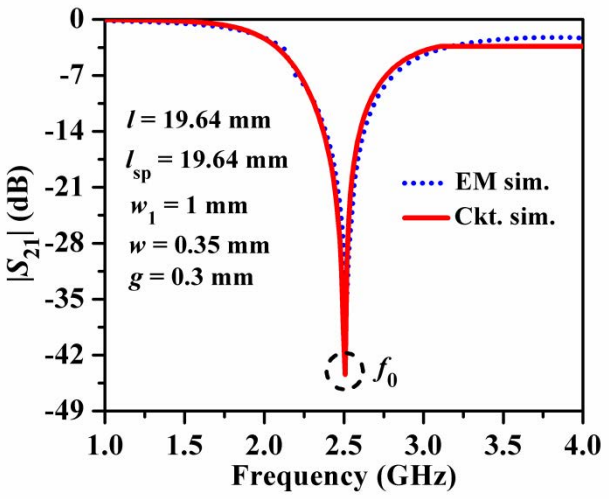

FIGURE 10. Resonant characteristics of L-shaped spurline.

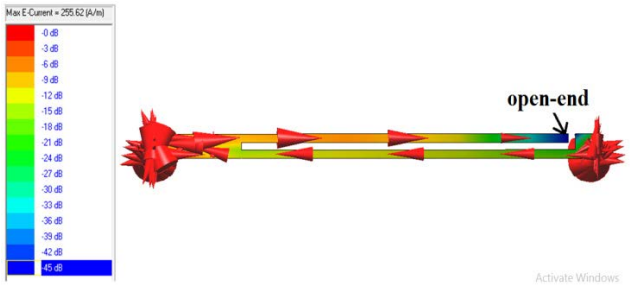

FIGURE 11. Distribution of surface current vectors L-spurline based quarter-wavelength line.

has been defined as $\alpha = l_{sp}/l$, where l is the length of the coupled line. Accordingly, the effects of different values of α on the even- and odd-mode resonant frequencies f_e and f_o have been exhibited in Fig. 13. For this study, the dimensions of the cells have been considered the same in Fig. 2 and the dimensions of the spurline have been considered as $g = 0.3$ mm, and the value of l_{sp} has been varied incrementally.

It has been revealed from Fig. 13 that f_o shifts more to lower frequency compared to f_e with the incremental value of α. Accordingly, the values of the modal resonant bandwidths have been obtained as $\Delta f = f_e\text{-}f_o = 0.29$ GHz for $\alpha = 0$ and $\Delta f_s = f_{es}\text{-}f_{os} = 0.17$ GHz for $\alpha = 1$. Thus, the modal resonant bandwidth has been reduced by 41.4% with spurline. This clearly justifies the ability of spurlines to achieve the modal phase velocity compensation, resulting in the suppression of harmonics. The investigations have been carried out further in Fig. 14(a)-(c) by varying

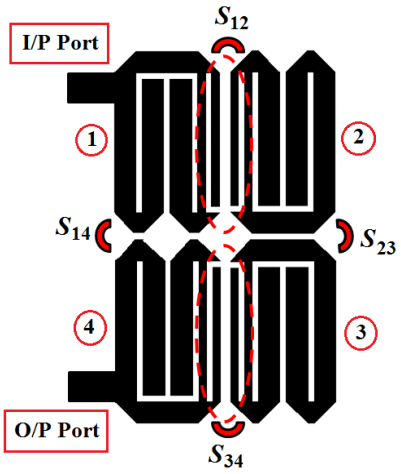

FIGURE 12. General layout of the fourth-order folded cross-coupled bandpass filter with L-shaped spurline.

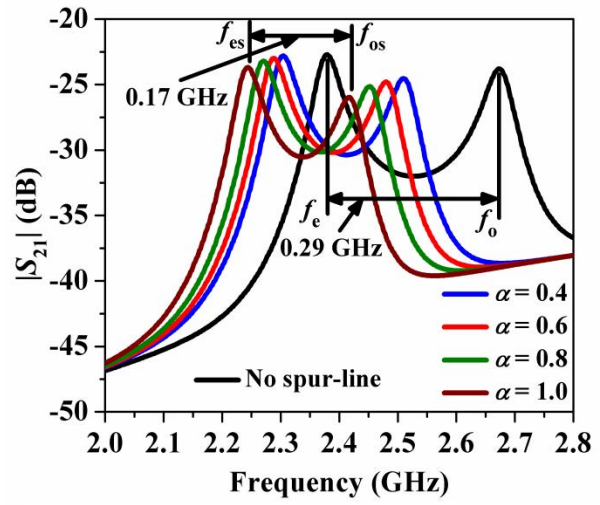

FIGURE 13. Passband characteristics of $|S_{21}|$ (dB) for a pair of folded cells in hybrid coupling configuration with L-spurline.

different coupling gaps S_{12} (mixed coupling), S_{23} (magnetic coupling), and S_{14} (electric coupling) respectively for the cross-coupled filter. For the entire study, one coupling gap has been varied keeping the dimensions of the other gaps unaltered as shown in Fig. 2. It has been revealed from Fig. 14(a) that the attenuation levels at f_{z1} and f_{z2} have been incremented; the insertion loss at f_0 has been incremented and the passband bandwidth has become narrower gradually with the incremental values of the coupling gap S_{12}. This indicates that as per the coupling scheme of the cross-coupled filter (1-2-3-4), the first coupling of the signal has occurred between the first and the second folded cells and it deteriorates with the increase of the coupling gap S_{12}. Thus, the value of S_{12} should be kept moderate for better response. The same phenomenon has happened in Fig. 14(b) for the increment of S_{23}. However, the increment of the insertion loss is more for the case of S_{23} than that for S_{12} due to the magnetic coupling. Thus, the value of S_{23} should be kept less for a better response. Accordingly, from Fig. 14(c) it has

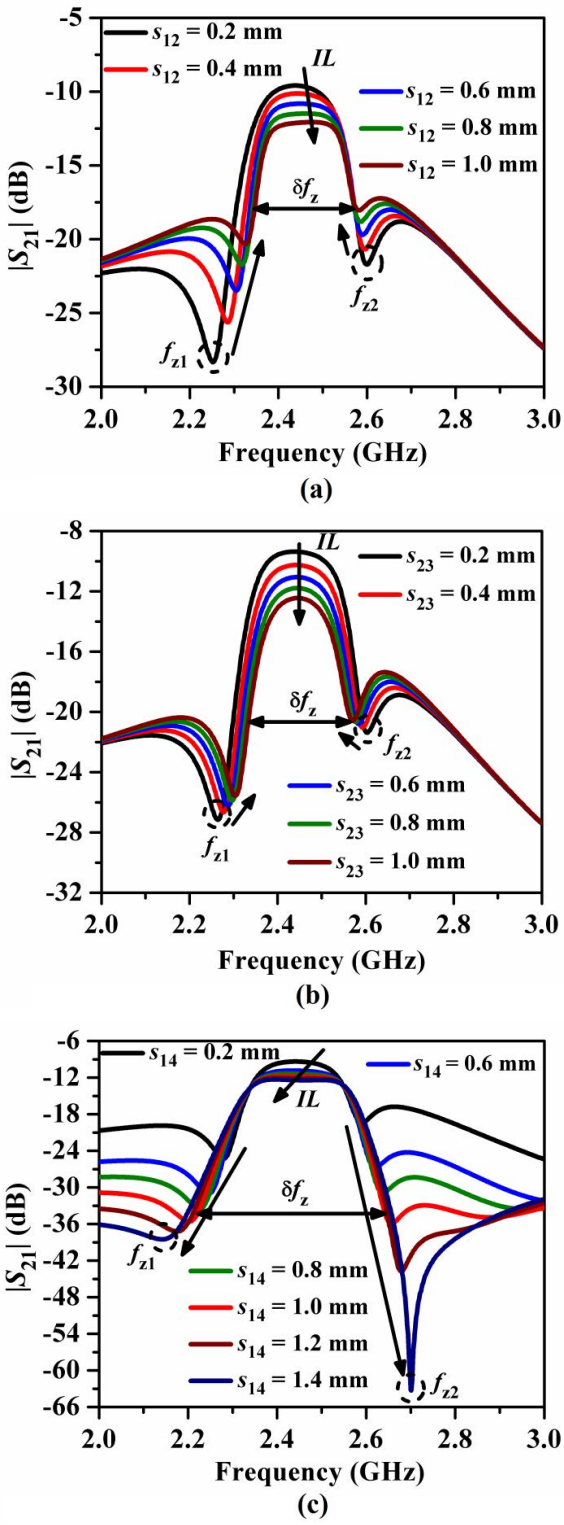

FIGURE 14. Passband variations for the folded cross-coupled filter with L-spurline for different coupling gaps variations: (a) $s_{12} = s_{34}$, (b) s_{23}, and (c) s_{14}.

been observed that a large value of S_{14} exhibits very sharp upper transmission zeroes deep with a large attenuation level. Moreover, there has been an insignificant variation in the

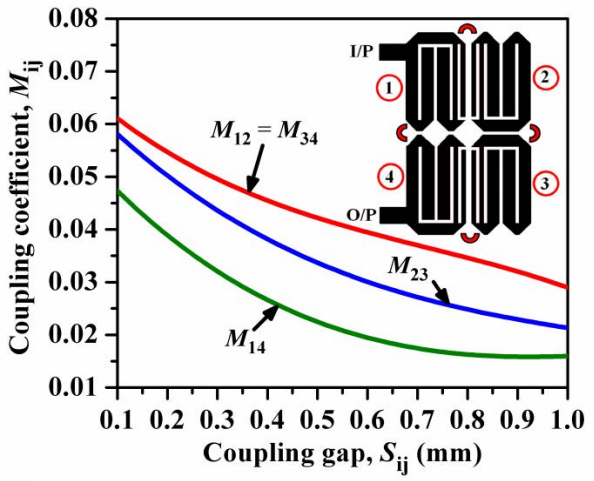

FIGURE 15. Variation of coupling-coefficient vs. coupling gap for a pair of folded cells with L-shaped spurline in different coupling configurations.

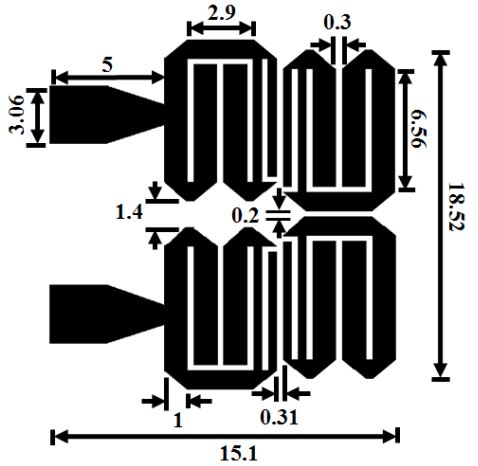

FIGURE 16. Layout of the fourth-order folded cross-coupled bandpass filter with L-shaped spurline. All dimensions are in mm.

insertion loss and the bandwidth due to the incremental values of S_{14} due to the electric coupling.

Fig. 15 illustrates the variation of the coupling coefficient vs. coupling gap for the cross-coupled filter with L-spurline. All the initial values of coupling gaps have been obtained from Fig. 15.

The final layout of the cross-coupled filter with optimized dimensions is shown in Fig. 16. The size of the filter is 279.65 mm^2 i.e., $0.22\lambda_g \times 0.27\lambda_g$. The wideband frequency response plots of $|S_{21}|$ and $|S_{11}|$ have been illustrated in Fig. 17(a)-(b) respectively. It has been observed from Fig. 17(a) that two sharp transmission zeros have occurred at 2.12 GHz and 2.72 GHz with attenuation levels of 47 dB and 53 dB respectively. Moreover, a wide stopband bandwidth up to $3.16f_0$ with a rejection level of 35 dB has been obtained. Accordingly, the attenuation levels of the harmonics for the cross-coupled filter without spurline have been suppressed by 25 dB. The passband insertion loss becomes limited to 1.1 dB and return loss becomes more than 18 dB. The passband return loss has been obtained as more than 20 dB

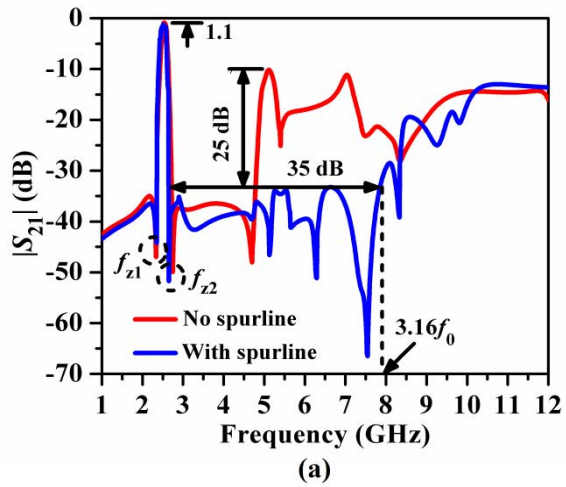

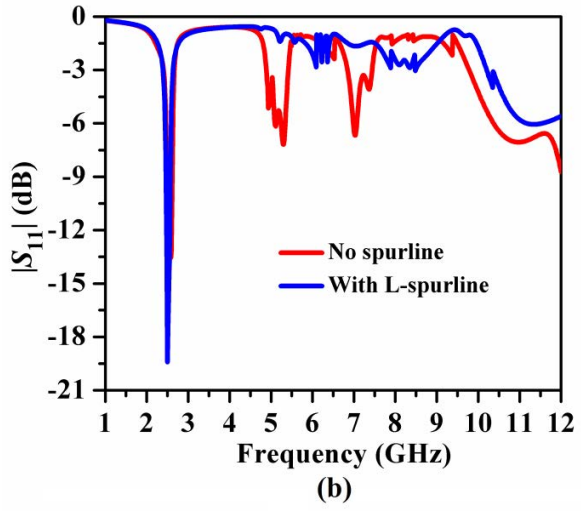

FIGURE 17. *S*-parameters plots of a fourth-order cross-coupled filter with L-spurline: (a) $|S_{21}|$ (dB), and (b) $|S_{11}|$ (dB) plots.

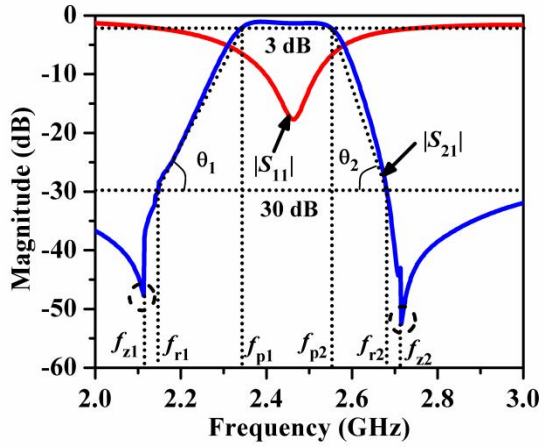

FIGURE 18. Calculation of shape factor and skirt selectivity factor for the cross-coupled filter with L-spurline.

as exhibited in Fig. 17(b). The values of *SF*, *ROSF*, and *TZSF* have been calculated from the passband response of Fig. 18 as $SF = 2.57$, $ROSF = 135$ dB/GHz for the lower passband edge, and 225 dB/GHz upper passband edge,

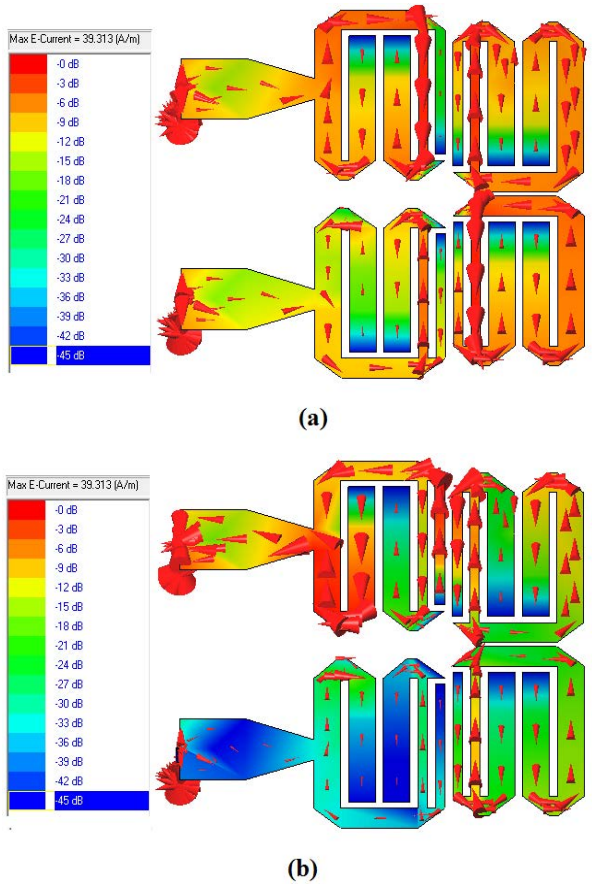

FIGURE 19. Distribution of surface current vectors for the fourth-order cross-coupled filter with L-spurline at (a) $f_0 = 2.5$ GHz, and (b) $2f_0 = 5.0$ GHz.

and $TZSF = 4.17$. It can be concluded that the frequency parameters' values with spurline have been improved over those without spurline, justifying the effectiveness of the spurline with respect to both the passband and the stopband. The surface current vectors distribution plots are highlighted in Fig. 19(a)-(b) at $f_0 = 2.5$ GHz and $2f_0 = 5.0$ GHz respectively. It has been observed that the surface current vectors have been propagated with large strength at 2.5 GHz due to the passband response. However, the strength of the current vectors has been diminished at 5.0 GHz at the output port due to the suppression of the harmonics' attenuation levels. By introducing the equivalent lumped elements circuit of spurline as shown in Fig. 9 into the cross-coupled filter of Fig. 5 between the coupled regions of two adjacent folded cells, the equivalent lumped elements circuit diagram of the cross-coupled filter with L-spurline has been obtained in Fig. 21. The values of the lumped elements have been computed as $L_1 = 2.226$ nH, $L_2 = 2.871$ nH, $L_3 = L_6 = 1.145$ nH, $L_4 = L_5 = 3.265$ nH, $C_{p1} = C_{p2} = 0.142$ pF, $C_{p3} = C_{p8} = 0.287$ pF, $C_{p4} = C_{p5} = 0.062$ pF, $C_{p6} = C_{p7} = 0.255$ pF, $C_{g1} = C_{g2} = C_{g3} = 0.012$ pF, $C_{14} = 0.012$ pF, $C_{12} = C_{34} = 0.031$ pF, $C_{23} = 0.218$ pF. The values of the spurline lumped elements have been computed as $L = 1.53$ nH, $C = 1.762$ pF, $R = 4.235$ kΩ.

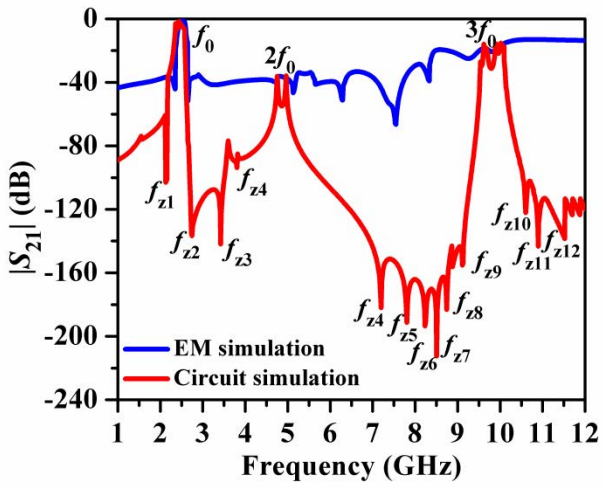

FIGURE 20. Comparison of EM and circuit simulated $|S_{21}|$ (dB) plot for the fourth-order cross-coupled filter with L-spurline.

The comparison between the EM and circuit simulated $|S_{21}|$ (dB) plots have been explored in Fig. 20. It has been observed that passbands are matched closely as Fig. 6. Moreover, twelve transmission zeros have occurred from 1.0 GHz to 12 GHz. It has been further revealed that the passband bandwidth of the filter has been reduced and the attenuation levels at the harmonics $2f_0$ and $3f_0$ have been suppressed due to the introduction of the spurline compared to that for the filter without spurline as highlighted in Fig. 6. This justifies the ability of the L-spurline in the suppression of harmonics. In the next section, the L-shaped spurline has been modified by a meander spurline [22] to provide slower wave effects for the odd-mode of EM wave and to achieve more suppression level of the harmonics along with a wider stopband.

V. HARMONICS SUPPRESSION BY MEANDER SPURLINE

From the previous section, it has been observed that the stopband attenuation level of the fourth-order cross-coupled filter has been limited to 35 dB and the stopband rejection bandwidth has been restricted to $3.16f_0$. However, the attenuation level increases gradually beyond $3.16f_0$ and becomes more than −15 dB. Thus, the presence of higher-order harmonics restricts the performance of the proposed filter for modern days wireless communication systems suitable for IoT. Accordingly, the next objective of the present work has been decided to reduce the stopband attenuation level further along with the extension of the stopband rejection bandwidth beyond $3.16f_0$. For this purpose, L-spurline has been replaced by meander spurline in which periodic slots with optimum dimensions have been placed alternately along the length of the coupled lines as highlighted in Fig. 22(a). The meander spurline is characterized by the slot width w_T, slot length l_T, slot gap g, periodicity p, and overall spurline length l_{sp}.

With this new slow-wave structure the overall electrical path of the odd-mode has been extended [18]. It causes more slowdown of the signal while propagating through

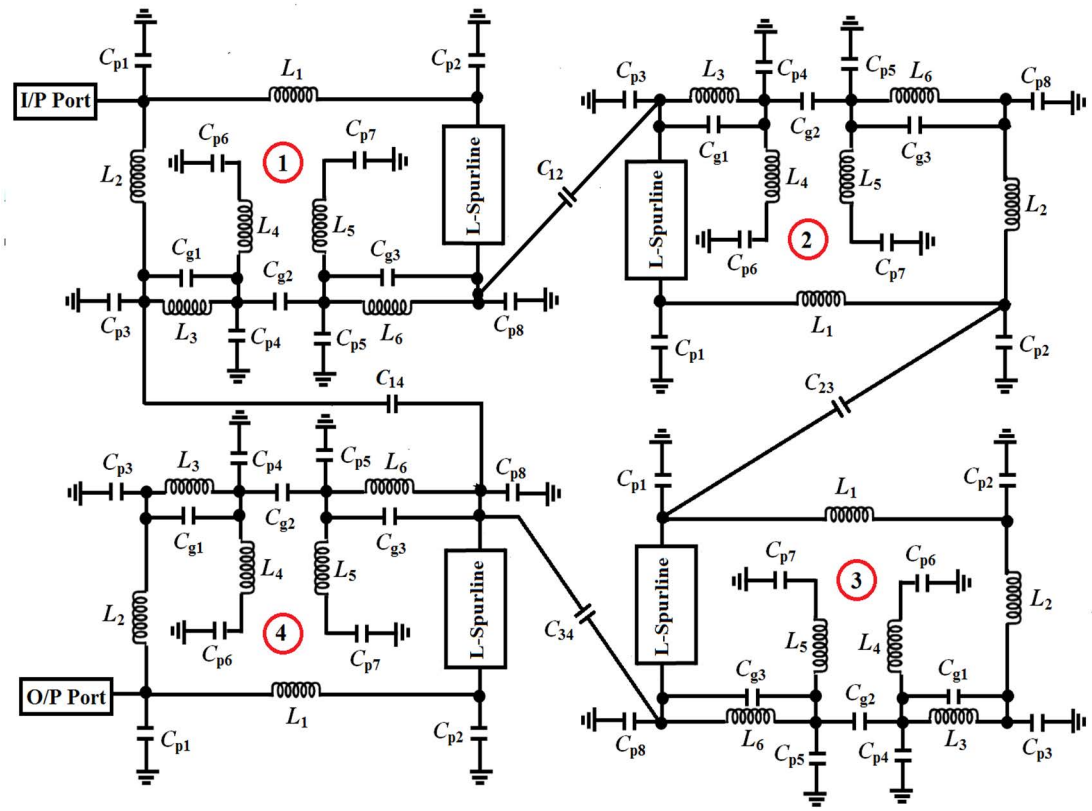

FIGURE 21. Equivalent lumped elements circuit diagram of the fourth-order cross-coupled bandpass filter with L-spurline.

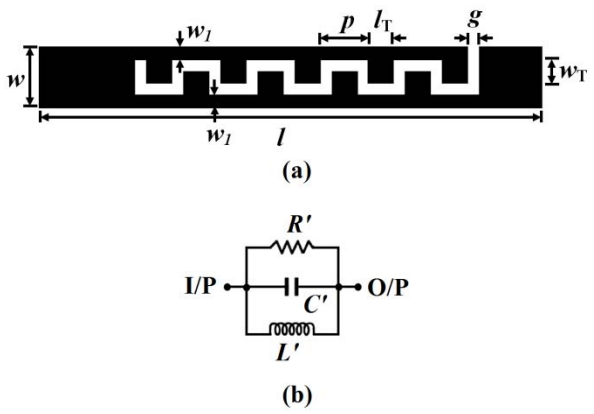

FIGURE 22. (a) Layout of a quarter-wavelength line with meander spurline, (b) equivalent lumped elements circuit diagram.

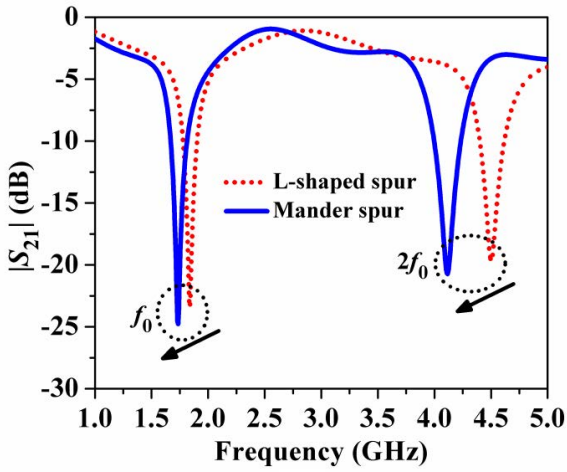

FIGURE 23. Comparison of $|S_{21}|$ (dB) plots between L- spurline and meander spurline based lines.

the central wiggle. However, the even-mode of the signal has been affected very little by this structure. In this way, a higher degree of modal phase velocity compensation has been achieved for the meander spurline-based line akin to the L-spurline-based line. Fig. 22(b) shows the equivalent lumped elements circuit diagram of the meander spurline. The lumped elements R', C', and L' have been obtained by following the same methodology as discussed in section 3 for the L-spurline. To understand the effects of such slowdown ability of the meander spurline, the comparison of the bandstop resonance characteristics of $|S_{21}|$ for the equivalent lumped elements circuit diagrams of meander spurline based and the L-spurline based quarter-wavelength lines has been performed in Fig. 23. It has been revealed that the attenuation levels at f_0 and $2f_0$ have decreased more compared to that for the L-spurline based line. Moreover, the passband bandwidth decreases due to the enhanced slow-wave effects and generation of additional capacitance couplings in the

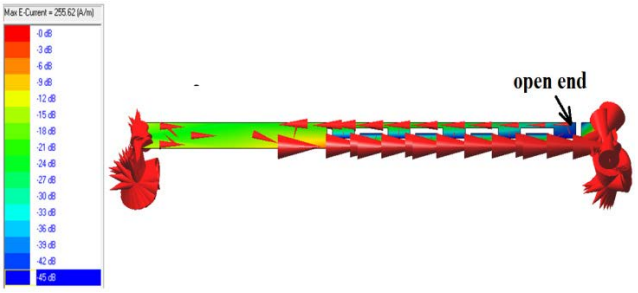

FIGURE 24. Distribution of surface current for a meander spurline based quarter-wavelength line.

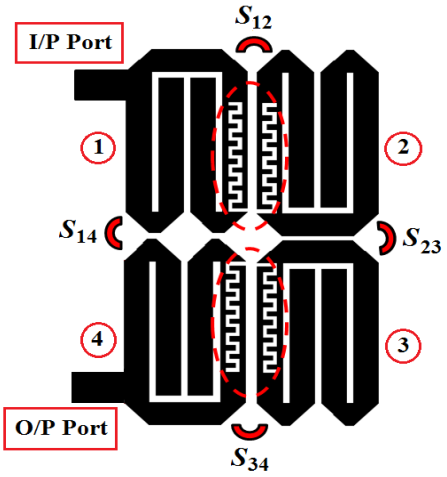

FIGURE 25. General layout of the fourth-order folded cross-coupled bandpass filter with meander spurline.

central meander path. The surface current distribution for a meander spurline-based quarter-wavelength line tuned at 2.5 GHz has been explored in Fig. 24. It has been observed that the current vectors have been concentrated more along the lower line segment and propagated towards the output port.

Moreover, very few current vectors have traveled along the upper line segment due to the open-end gap. This clearly justifies the enhanced slow-wave nature of the meander spurline over the L-spurline. Subsequently, such a meander spurline has been incorporated in the folded cells of the cross-coupled filter in place of the L-spurline as highlighted in Fig. 25. From the passband characteristics as shown in Fig. 26 for a pair of folded cells in a hybrid coupling configuration, it has been observed that the bandwidth between the even- and odd-mode resonant frequencies gradually decreases with a higher rate as the number of periodic slots N has been incremented.

This justifies the enhanced slow-wave nature of the meander spurline over the L-shaped spurline. Accordingly, the effects of the variations of different coupling gaps for the cross-coupled filter with a meander spurline have been exhibited in Fig. 27(a)-(c).

For the incremental values of S_{12} in mm (mixed-coupling) the insertion loss increases and the attenuation level at f_{z1}

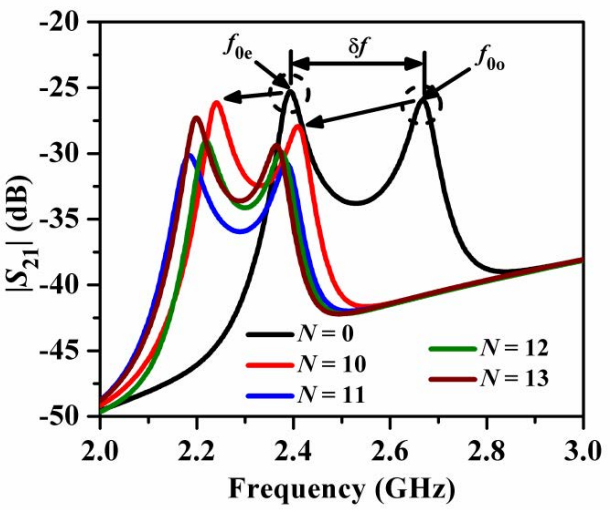

FIGURE 26. Passband characteristics of $|S_{21}|$ (dB) for a pair of folded cells in hybrid coupling configuration with meander spurline.

and f_{z2} have been incremented along with a reduction in passband bandwidth. The same phenomenon has taken place for the increment of S_{23} values in mm (magnetic coupling). However, for the incremental values of S_{12} (mm) (electric coupling), the reverse phenomenon has occurred i.e., the attenuation levels at f_{z1} and f_{z2} have been decremented along with the extension of the bandwidth. Thus, the values of S_{12} and S_{23} should be considered small, whereas the value of S_{14} should be considered large enough to achieve satisfactory passband performance for the cross-coupled bandpass filter Accordingly, the initial values of these coupling gaps have been determined from the design curves of coupling coefficients vs. coupling gaps as shown in Fig. 28. The final layout of the cross-coupled filter with optimized dimensions has been depicted in Fig. 29. The overall size of the filter is 270.6 mm^2 i.e., $0.22\lambda_g \times 0.26\lambda_g$. Accordingly, the comparisons of the simulated S-parameters plot for the fourth-order cross-coupled filters without spurline and with meander spurline have been performed in Fig. 30(a)-(b). From Fig. 30(a), it has been observed that two sharp transmission zeros f_{z1} and f_{z2} have occurred at 2.3 GHz and 2.7 GHz with the attenuation levels of 38 dB and 55 dB respectively. The passband insertion loss becomes 1.04 dB. Moreover, a wide stopband with a rejection level of 34 dB up to $3.88f_0$ and 26 dB up to $4.8f_0$ has been obtained. Hence, the harmonics' attenuation levels have been suppressed by 24 dB with the meander spurline over the filter without spurline.

From Fig. 30(b) it can be noticed that the passband bandwidth becomes narrower with the return loss better than 25 dB. The closure look of the passband response has been highlighted in Fig. 31. From the plot the values of *SF*, *ROSF*, and *TZSF* have been calculated as $SF = 5.5$, $ROSF = 122.73$ dB/GHz for the lower passband edge and 192.86 dB/GHz upper passband edge and $TZSF = 4.8$. It indicates that the skirt selectivity of the filter has been improved over L-spurline-based filter. The

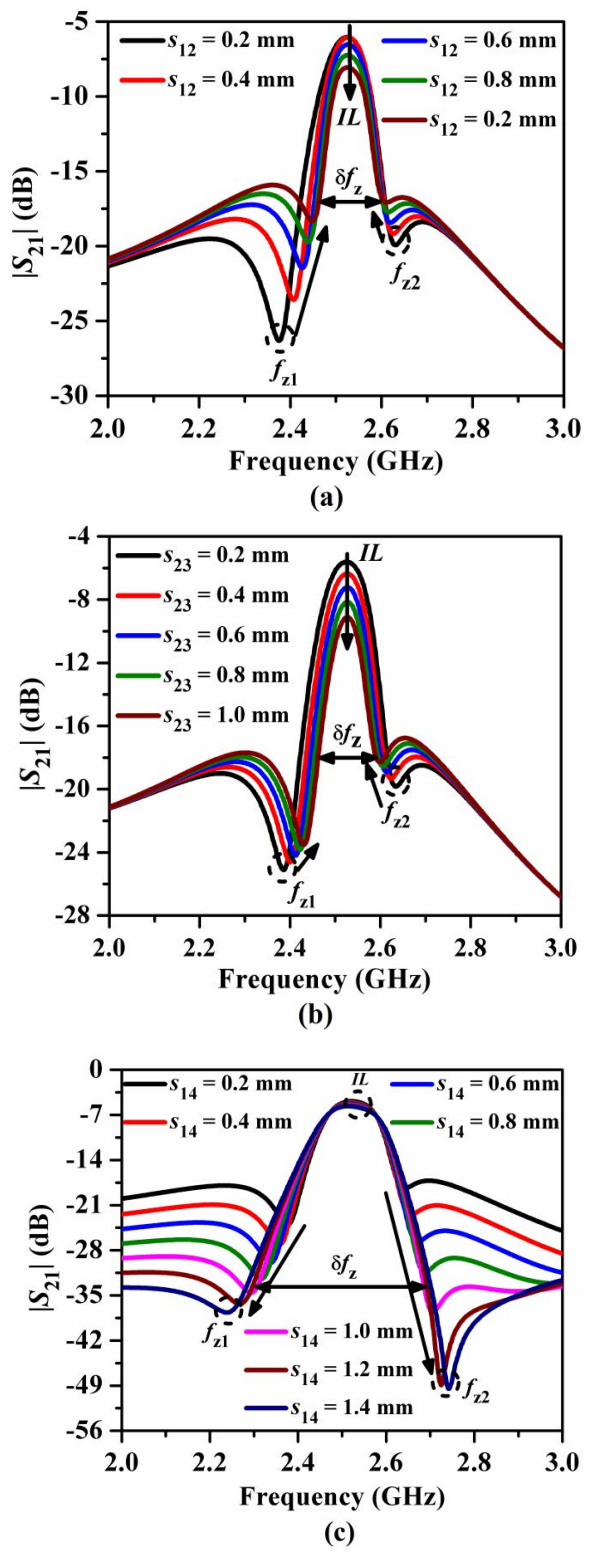

FIGURE 27. Passband variations for the folded cross-coupled filter with meander spurline for different coupling gaps variations: (a) $s_{12} = s_{34}$, (b) s_{23}, and (c) s_{14}.

distribution of the surface current vectors for the meander spurline-based cross-coupled filter has been highlighted in Fig. 32(a)-(b) at $f_0 = 2.5$ GHz and $2f_0 = 5.0$ GHz

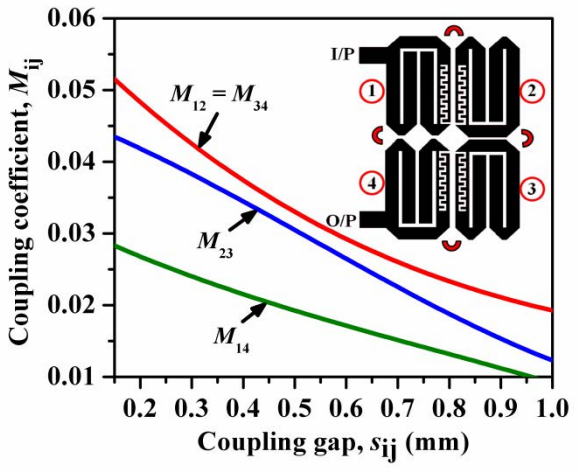

FIGURE 28. Variation of coupling-coefficient vs. coupling gap for a pair of folded cells with mender spurline in different coupling configurations.

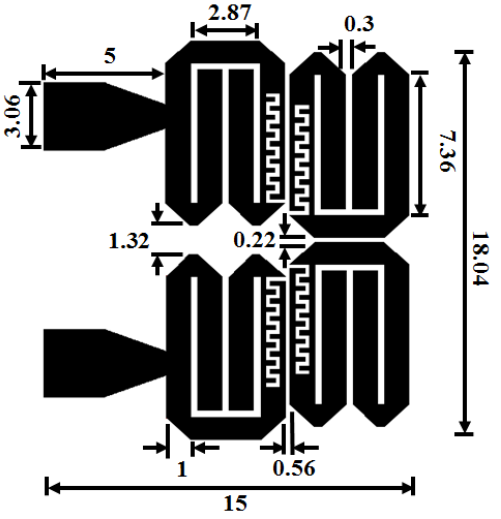

FIGURE 29. Layout of the fourth-order folded cross-coupled bandpass filter with meander spurline. All dimensions are in mm.

respectively. It has been revealed from Fig. 32(a) that the surface current vectors have been concentrated strongly through the central meander wiggle and have reached the output port with large strength at 2.5 GHz due to the passband response. However, their distributions have been diminished greatly at 5.0 GHz (Fig. 32(b)) due to the suppression of the harmonics' attenuation levels by the spurline. However, their distributions have been diminished greatly at 5.0 GHz due to the suppression of the harmonics' attenuation levels by the spurline. The lumped elements circuit diagram of the cross-coupled filter with a meander spurline has been depicted in Fig. 33. The values of the lumped elements have been computed by following the conventional transmission line theory [1]. The values are as $L_1 = 2.115$ nH, $L_2 = 2.325$ nH, $L_3 = L_6 = 1.101$ nH, $L_4 = L_5 = 2.965$ nH, $C_{p1} = C_{p2} = 0.121$ pF, $C_{p3} = C_{p8} = 0.262$ pF, $C_{p4} = C_{p5} = 0.048$ pF, $C_{p6} = C_{p7} = 0.185$ pF, $C_{g1} = C_{g2} = C_{g3} = 0.01$ pF, $C_{14} = 0.008$ pF,

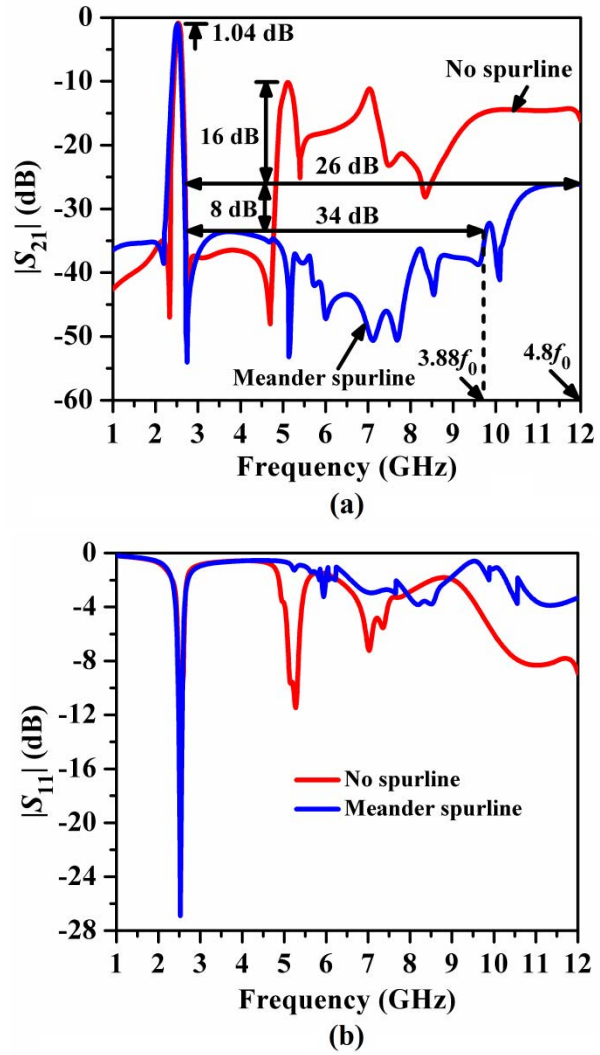

FIGURE 30. *S*-parameters plots of a fourth-order cross-coupled filter with meander spurline: (a) $|S_{21}|$ (dB), and (b) $|S_{11}|$ (dB) plots.

$C_{12} = C_{34} = 0.025$ pF, $C_{23} = 0.201$ pF. The values of the meander spurline lumped elements have been computed as $L' = 2.319$ nH, $C' = 1.738$ pF, $R' = 3.448$ kΩ corresponding to the value of $|S_{21}|$ as 26 dB from Fig. 23. The circuit simulated $|S_{21}|$ (dB) plot has been compared with that of the EM simulated plot in Fig. 34. It has been observed that passbands are matched closely as expected and fourteen transmission zeros have been obtained from 1.0 GHz to 12 GHz for the circuit simulation plot. Moreover, it has been revealed that the attenuation level at $2f_0$ and $3f_0$ has been suppressed greatly.

It has been also revealed from Fig. 34 that more transmission zeros have occurred in the stopband than that in Fig. 20 due to the enhanced slow-wave effects of meander spurline over conventional L-spurline.

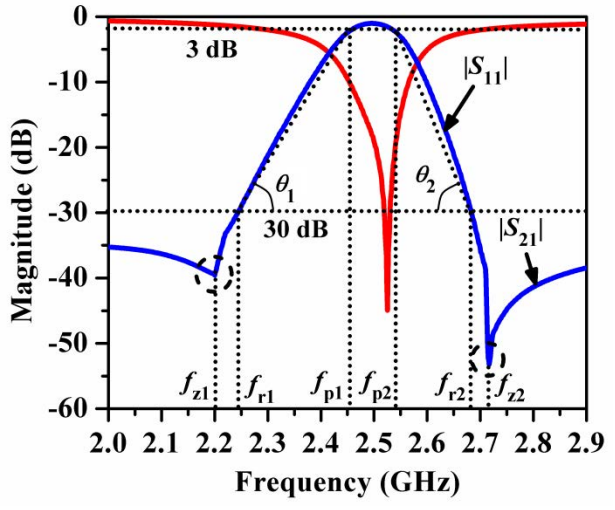

FIGURE 31. Calculation of shape factor and skirt selectivity factor for the cross-coupled filter with meander spurline.

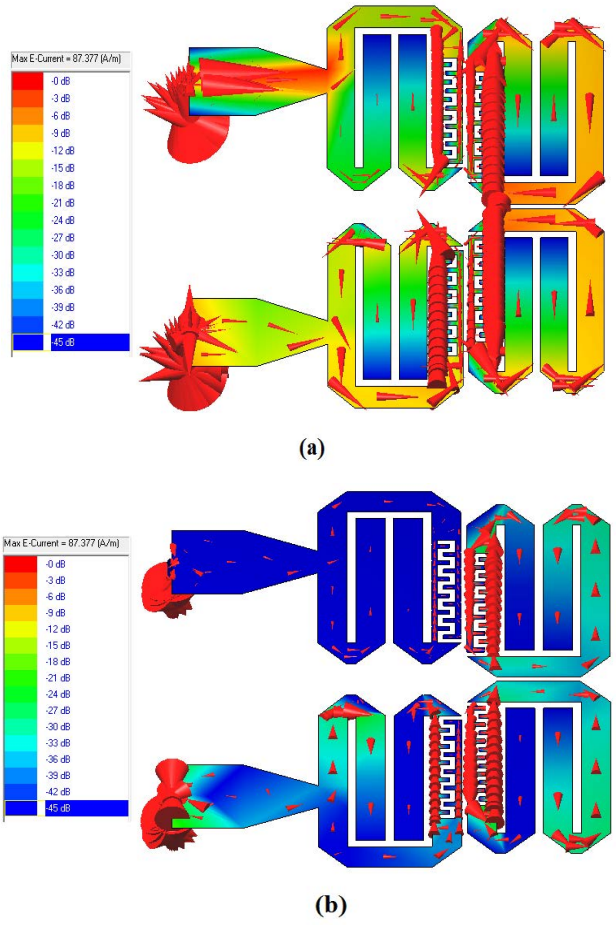

FIGURE 32. Distribution of surface current vectors for the fourth-order cross-coupled filter with meander-spurline at (a) $f_0 = 2.5$ GHz, and (b) $2f_0 = 5.0$ GHz.

VI. EXPERIMENTAL RESULTS

In order to validate the performance of the proposed cross-coupled filters with the spurline, two prototypes have been fabricated on FR4 laminate with tin plating to avoid abrasion due to environmental conditions and also to provide ruggedness and protection as shown in Fig. 35(a)-(b).

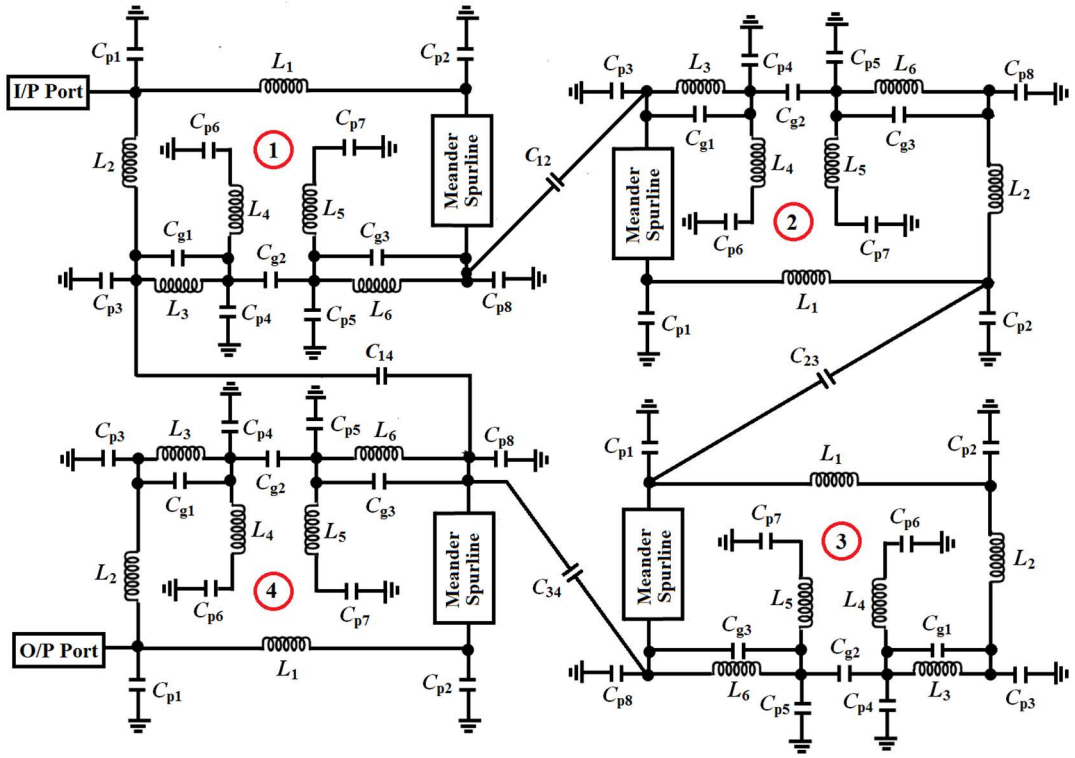

FIGURE 33. Equivalent lumped elements circuit diagram of the fourth-order cross-coupled bandpass filter with meander spurline.

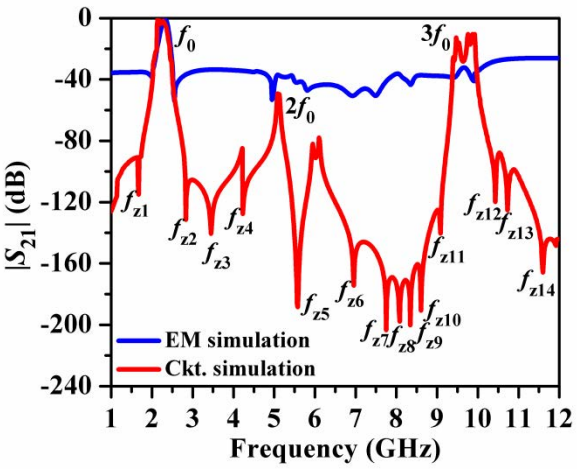

FIGURE 34. Circuit vs. EM simulated $|S_{21}|$ (dB) plot for the fourth-order cross-coupled bandpass filter with meander spurline.

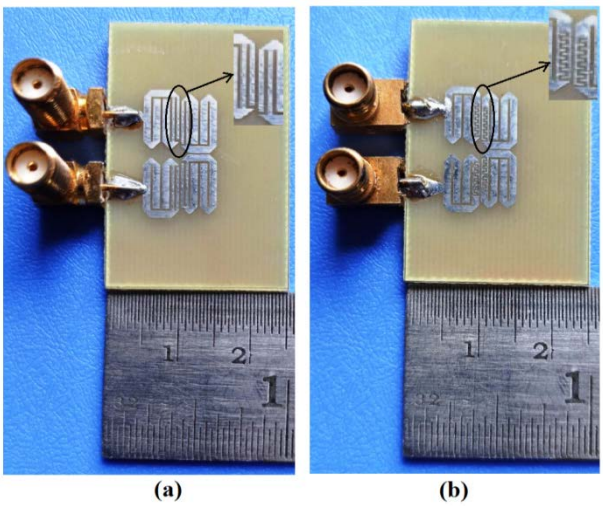

FIGURE 35. Fabricated prototypes of the fourth-order cross-coupled bandpass filters with (a) L-spurline and (b) meander spurline.

The testing of the prototypes has been carried out with the N9928A vector network analyzer of Keysight Technologies in a closed environment and the comparison of the measured *S*-parameters plots with that of the simulated results has been performed in Fig. 36(a)-(b) for L-spurline based filter and Fig. 37(a)-(b) for meander spurline based filter respectively. It has been observed from Fig. 36(a) that a wide stopband of 35 dB up to $3.76f_0$ has been obtained and accordingly, the harmonics' attenuation levels have been suppressed by 25 dB.

Besides, the measured passband response has been matched closely with an insertion loss of 1.2 dB. Moreover, multiple transmission zeros have been occurred in the stopband, indicating the improvement of the stopband rejection. The return loss has been measured as 20 dB from Fig. 36(b). Subsequently, from Fig. 37(a) it has been observed that the skirt selectivity of the passband for the cross-coupled filter with a meander spurline has been improved significantly by the generation of the transmission zeros at the passband edges with attenuation levels greater than 45 dB. Moreover, a wide stopband of rejection level 38 dB up to $4f_0$ and

TABLE 2. Comparison of similar works.

Designs	*FBW* (%)	f_0 (GHz)	*IL* (dB)	*RL* (dB)	*SRL* (dB)	*SBW* (GHz)	*No. of TZs*	Size ($\lambda_g \times \lambda_g$) (mm^2)
L-shaped spurline	4	2.5	1.2	25	35	$3.76f_0$	9	0.22 × 0.27
Meander spurline			1.15	22	38	$4f_0$	12	0.22 × 0.26
[8]	9	1.46	1.3	17	26	$3.2f_0$	5	0.17 × 0.10
[10]	36	2.5	0.6	15	40	2.4	3	0.21 × 0.18
[11]	8.4	5.1	2.2	20	24.5	$4.9f_0$	14	0.24 × 0.35
[12]	39	2.1	0.8	20	29.5	$2.3f_0$	6	0.39 × 0.36
[13]	11.5	3.5	1.7	13	30	$3f_0$	7	0.21 × 0.18
[14]	44.5	10.8	0.6	20	20	$4f_0$	4	0.16 × 0.75
[15]	6.1	10	0.9	20	20	$4f_0$	3	0.14 × 0.92
[18]	4	2.5	1.8	16	40	$4f_0$	12	0.49 × 0.17
[20]	4	2.5	1.6	13	38	$4.48f_0$	12	0.62 × 0.12

FBW = fractional bandwidth, *IL* = insertion loss, *RL* = return loss, *SRL* = stopband rejection level, *SBW* = stopband bandwidth.

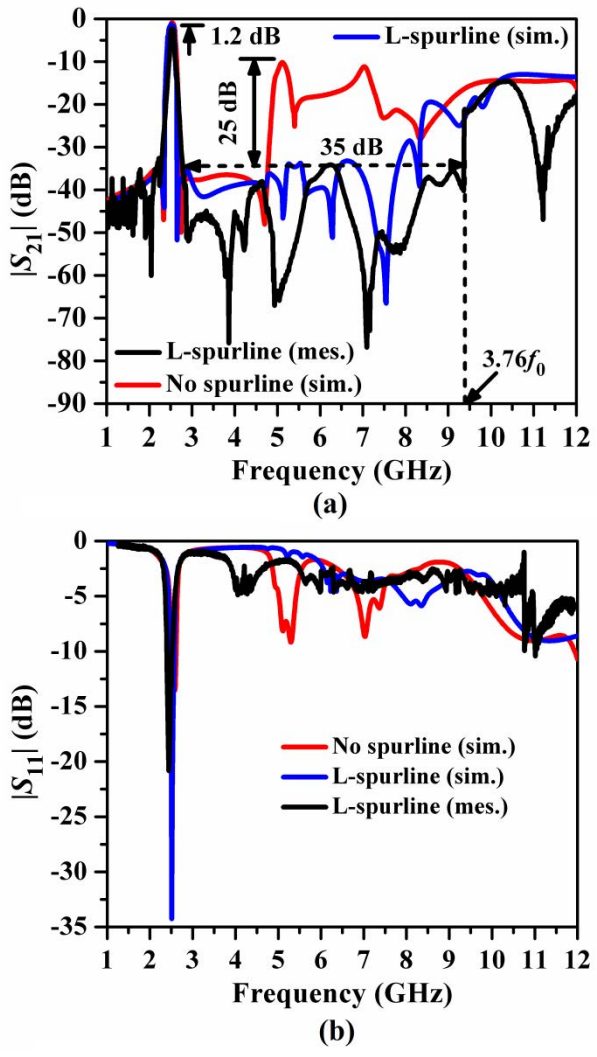

FIGURE 36. Comparison of simulated vs. measured S-parameters plots for the fourth-order cross-coupled filter with L-spurline: (a) $|S_{21}|$ (dB) and (b) $|S_{11}|$ (dB).

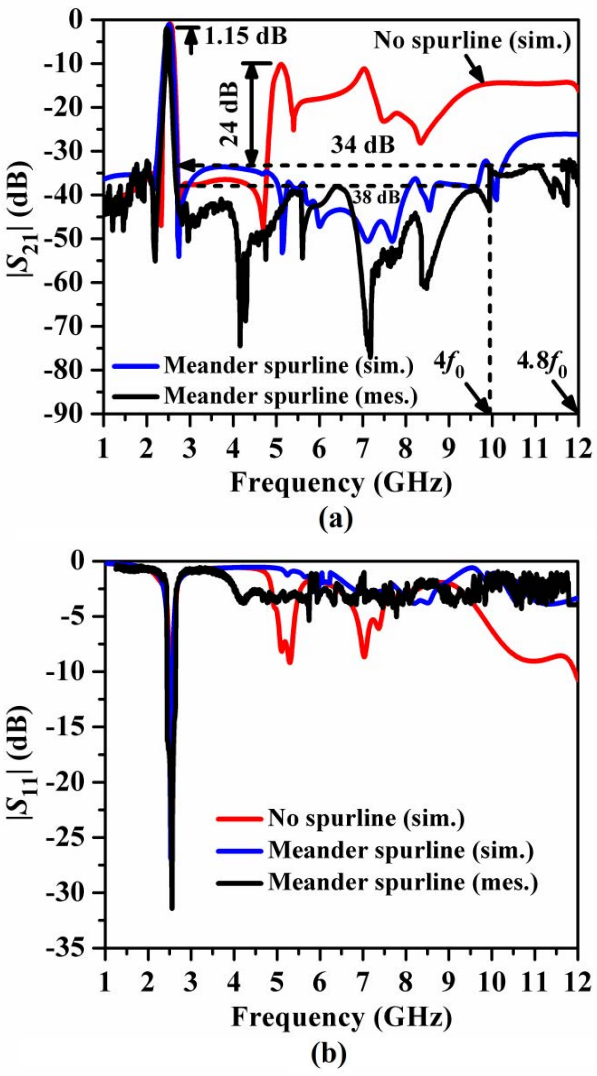

FIGURE 37. Comparison of simulated vs. measured S-parameters plots for the fourth-order cross-coupled filter with meander-spurline: (a) $|S_{21}|$ (dB) and (b) $|S_{11}|$ (dB).

34 dB up to $4.8f_0$ have been obtained in measurement. For this filter, multiple transmission zeros have generated in the stopband with attenuation levels greater than 50 dB on average. It clearly justifies the ability of the meander spurline

for improved harmonics suppression performance over the L-spurline based filter.

Moreover, from Fig. 37(b), it can be noticed that the return loss becomes more than 25 dB. It can be concluded from the experimental results for both the filters that the meander spurline-based filter exhibits better harmonics suppression performance over the L-spurline-based filter. Table 2 compares the experimental results of the present work with other similar works. It has been revealed that the proposed filters have exhibited more stopband rejection levels compared to [8], [11]–[15] and more stopband bandwidth over [8], [10], [12], and [13]. Moreover, the proposed filters have occupied less circuit area over [11], [12], [14], [15], [18], and [20]. The insertion loss becomes less than [13], [18], [20] for the same FR4 substrate and the return loss becomes greater than all the other works included in the table. It has been further noted that more transmission zeros have been generated for the proposed filters than [8], [10], [12–[15].

Thus, it can be concluded that the proposed filters exhibit improvement with respect to the skirt selectivity, return loss, stopband rejection level, stopband rejection bandwidth, generation of more number of transmission zeros, and overall circuit area in terms of guided wavelength λ_g centered at f_0.

VII. CONCLUSION

The present paper illustrates the design of a fourth-order cross-coupled bandpass filter with harmonics suppression performance with spurline. First, the open-loop hairpin resonators have been folded twice and then placed in a cross-coupled configuration. Accordingly, the skirt selectivity of the filter has been improved and the size of the filter has been reduced by 17%. However, the attenuation levels of the harmonics have become more than -10 dB. Later, the coupled arms of the adjacent folded cell have been perturbed by L-spurline with optimum dimensions and as a result, the stopband rejection level of 35 dB up to $3.76f_0$ has been obtained. In order to achieve more stopband rejection, L-spurline has been modified by the meander spurline. Meander spurline offers more slow-wave performance and accordingly, a wide stopband with the suppression level of 38 dB up to $4f_0$ has been obtained. The size of the final filter exhibits a size reduction of 33% over the conventional open-loop resonator cross-coupled filter. The proposed filter is suitable for modern IoT-based WLAN systems.

REFERENCES

[1] J.-S. Hong and M. J. Lancaster, "Advanced RF/microwave filters," in *Microstrip Filter for RF/Microwave Applications*. New York, NY, USA: Wiley, 2001, pp. 315–321.

[2] X.-B. Ma and T. Jiang, "Wideband bandpass filter with controllable bandwidth and high selectivity using two different types of resonators," *Microw. Opt. Technol. Lett.*, vol. 57, no. 6, pp. 1319–1323, Jun. 2015.

[3] M. Caenepeel, F. Seyfert, Y. Rolain, and M. Olivi, "Parametric modeling of the coupling parameters of planar coupled-resonator microwave filters," in *Proc. Eur. Microw. Conf. (EuMC)*, Sep. 2015, p. 4.

[4] J. K. Ali and H. T. Ziboon, "Design of compact bandpass filters based on fractal defected ground structure (DGS) resonators," *Indian J. Sci. Technol.*, vol. 9, no. 39, pp. 1–9, Oct. 2016.

[5] C. Schuster, R. Hu, A. Wiens, M. Maasch, R. Jakoby, and H. Maune, "Cross-coupled open-loop resonator bandpass filter with independently tunable center frequency and bandwidth," in *Proc. IEEE Radio Wireless Symp. (RWS)*, Jan. 2018, pp. 52–55.

[6] X. Guan, S. Xie, B. Ren, and X. Li, "Compact four-pole wideband bandpass filter with mixed electric and magnetic coupling," *Microw. Opt. Technol. Lett.*, vol. 62, no. 6, pp. 2178–2182, Jun. 2020.

[7] M. T. E. Khorassani, H. Benchakroun, I. Badaout, A. Farkhsi, and N. A. Touhami, "Design of cross-coupled band-pass filter based on square open loop resonators," *Int. J. Microw. Opt. Technol.*, vol. 15, no. 6, pp. 511–516, Nov. 2020.

[8] N. Kumar and Y. K. Singh, "Compact stub-loaded open-loop BPF with enhanced stopband by introducing extra transmission zeros," *Electron. Lett.*, vol. 51, no. 2, pp. 164–166, 2015.

[9] X. Rao, T. Huang, Y. M. Huang, and H. Jin, "Size-miniaturized bandpass filter made of folded stepped-impedance resonators with adjacent and nonadjacent coupling for selectivity enhancement," in *Proc. Prog. Electromagn. Res. Symp. Fall (PIERS–FALL)*, Nov. 2017, pp. 3045–3048.

[10] J. Xu, F. Xiao, Y. Cao, Y. Zhang, and X. H. Tang, "Compact microstrip filter with third-order quasi-elliptic bandpass response," *IEEE Access*, vol. 6, pp. 63375–63381, 2018.

[11] C. Han, Y. Rao, H. J. Qian, and X. Luo, "High-selectivity bandpass filter with wide upper stopband using harmonic suppression structure," in *Proc. IEEE Int. Symp. Radio-Freq. Integr. Technol. (RFIT)*, Aug. 2019, pp. 1–3.

[12] S. Lu, K. Xu, Y. Guo, Y. Ren, and Q. Chen, "Bandpass filter using coupled-line-+stub cascaded structure with high stopband rejection," *Microw. Opt. Technol. Lett.*, vol. 63, no. 1, pp. 69–74, Jan. 2021.

[13] T. Huang and Z. Shao, "A size-miniaturized bandpass filter with selectivity-enhanced and high harmonic suppression performance," *Int. J. Microw. Wireless Technol.*, vol. 9, no. 9, pp. 1809–1815, Nov. 2017.

[14] T. Huang, Z. H. Shao, and Z. Chen, "Miniaturized wideband bandpass filter with enhanced selectivity and stopband suppression," *Microw. Opt. Technol. Lett.*, vol. 60, no. 3, pp. 769–772, Mar. 2018.

[15] F. Yan, Y. M. Huang, T. Huang, S. Ding, K. Wang, and M. Bozzi, "Transversely compact single-ended and balanced bandpass filters with source–load-Coupled spurlines," *Electronics*, vol. 8, no. 4, p. 416, Apr. 2019.

[16] T. K. Das and S. Chatterjee, "Harmonic suppression in a folded hairpin-line cross-coupled bandpass filter by using spur-line," in *Proc. Devices Integr. Circuit (DevIC)*, May 2021, pp. 474–478.

[17] S. F. Chang, W. L. Chen, S. C. Chang, C. K. Tu, C. L. Wei, C. H. Chien, C. H. Tsai, J. Chen, and A. Chen, "A dual-band RF transceiver for multistandard WLAN applications," *IEEE Trans. Microw. Theory Techn.*, vol. 53, no. 3, pp. 1048–1055, Mar. 2005.

[18] T. K. Das and S. Chatterjee, "Multi-spurious harmonics suppression in folded hairpin line bandpass filter by meander spur-line," *Int. J. RF Microw. Comput.-Aided Eng.*, vol. 31, no. 11, Nov. 2021, Art. no. e22858, doi: 10.1002/mmce.22858.

[19] T. K. Das and S. Chatterjee, "Harmonic suppression by using T-shaped spur-line in a compact hairpin-line bandpass filter," *Radioengineering*, vol. 30, no. 2, pp. 296–303, Jun. 2021, doi: 10.13164/re.2021.0296.

[20] T. K. Das and S. Chatterjee, "Spurline-embedded compact hairpin-line bandpass filters for wide harmonic suppression," *Int. J. Microw. Wireless Technol.*, vol. 14, no. 5, pp. 553–565, Jun. 2022, doi: 10.1017/S1759078721001197.

[21] R. N. Bates, "Design of microstrip spur-line band-stop filters," *IEE J. Microw., Opt. Acoust.*, vol. 1, no. 6, pp. 209–214, Nov. 1977.

[22] C. Nguyen and C. Hsieh, "Millimeter wave printed circuit spurline filters," in *IEEE MTT-S Int. Microw. Symp. Dig.*, May 1983, pp. 98–100.

TARUN KUMAR DAS was born in Kolkata, India, in 1979. He received the B.Tech. degree in ECE from Kalyani University, in 2003, and the M.Tech. degree in software engineering from WBUT, Kolkata, in 2008. He is currently pursuing the Ph.D. degree with Jadavpur University. He is also an Assistant Professor with the ECE Department, Future Institute of Engineering and Management, Kolkata. His research interest includes harmonic suppression in microwave filters.

SAYAN CHATTERJEE (Senior Member, IEEE) was born in Kolkata, India, in 1980. He received the B.E. degree (Hons.) in ECE from Vidyasagar University, India, in 2003, and the M.E. degree in ETCE and the Ph.D. degree in engineering from Jadavpur University, Kolkata, in 2005 and 2015, respectively. He has worked as a Scientist at SAMEER, Kolkata, from 2005 to 2009. He is currently working as a Professor with the ETCE Department, Jadavpur University. He has worked as the Secretary and a Treasurer of IEEE Kolkata Section, from 2014 to 2017. His research interests include microwave and millimeter wave antennas, SIW technology, design of microwave passive devices, and design of waveguide-based slotted array antenna. He was awarded outstanding volunteer for his service in IEEE Kolkata Section, in 2014 and 2019. He is a member of the IEEE Special Interest Group on Humanitarian Technology (SIGHT), Institute of Engineers, Universal Association of Computer and Electronics Engineers.

SHARUL KAMAL ABDUL RAHIM (Senior Member, IEEE) received the degree in electrical engineering from The University of Tennessee, USA, the M.Sc. degree in engineering (communication engineering) from Universiti Teknologi Malaysia (UTM), and the Ph.D. degree in wireless communication system from the University of Birmingham, U.K., in 2007. After his graduation from The University of Tennessee, he spent three years in industry. After graduating the M.Sc. degree, he joined UTM, in 2001, where he is currently a Professor with the Wireless Communication Center. He has published over 200 learned articles, including *IEEE Antenna and Propagation Magazine*, the IEEE TRANSACTIONS ON ANTENNA AND PROPAGATION, IEEE ANTENNA AND PROPAGATION LETTERS, and obtained various patents. His research interests include antenna design, smart antenna systems, beam forming networks, and microwave devices for fifth generation mobile communication. He is also a Senior Member of IEEE Malaysia Section, a member of The Institute of Engineers, Malaysia, a Professional Engineer with BEM, a member of the Eta Kappa Nu Chapter, The University of Tennessee, and the International Electrical Engineering Honor Society. He is also an Executive Committee of the IEM Southern Branch.

TAN KIM GEOK received the B.E., M.E., and Ph.D. degrees in electrical engineering from the University of Technology Malaysia, Malaysia, in 1995, 1997, and 2000, respectively. He has been a Senior Research and Development Engineer at EPCOS, Singapore, in 2000. In 2001 and 2003, he joined the DoCoMo Euro-Laboratories, Munich, Germany. He is currently an Academic Staff at Multimedia University. His research interests include radio propagation for outdoor and indoor, RFID, multi-user detection technique for multi-carrier technologies, and A-GPS.